Structural History of Human SRGAP2 Proteins

Michael Sporny,[†,1] Julia Guez-Haddad,[†,1] Annett Kreusch,[2] Sivan Shakartzi,[1] Avi Neznansky,[1] Alice Cross,[3] Michail N. Isupov,[3] Britta Qualmann,[2] Michael M. Kessels,[2] and Yarden Opatowsky*[,1]

[1]The Mina & Everard Goodman Faculty of Life Sciences, Bar-Ilan University, Ramat Gan, Israel

[2]Institute for Biochemistry I, Jena University Hospital, Friedrich Schiller University Jena, Jena, Germany

[3]Department of Biosciences, College of Life and Environmental Sciences, University of Exeter, Exeter, United Kingdom

[†]These authors contributed equally to this work.

***Corresponding author:** E-mail: yarden.opatowsky@biu.ac.il.

Associate editor: Banu Ozkan

Abstract

In the development of the human brain, human-specific genes are considered to play key roles, conferring its unique advantages and vulnerabilities. At the time of *Homo* lineage divergence from *Australopithecus*, *SRGAP2C* gradually emerged through a process of serial duplications and mutagenesis from ancestral *SRGAP2A* (3.4–2.4 Ma). Remarkably, ectopic expression of *SRGAP2C* endows cultured mouse brain cells, with human-like characteristics, specifically, increased dendritic spine length and density. To understand the molecular mechanisms underlying this change in neuronal morphology, we determined the structure of SRGAP2A and studied the interplay between SRGAP2A and SRGAP2C. We found that: 1) SRGAP2A homo-dimerizes through a large interface that includes an F-BAR domain, a newly identified F-BAR extension (Fx), and RhoGAP-SH3 domains. 2) SRGAP2A has an unusual inverse geometry, enabling associations with lamellipodia and dendritic spine heads *in vivo*, and scaffolding of membrane protrusions in cell culture. 3) As a result of the initial partial duplication event (∼3.4 Ma), SRGAP2C carries a defective Fx-domain that severely compromises its solubility and membrane-scaffolding ability. Consistently, SRGAP2A:SRAGP2C hetero-dimers form, but are insoluble, inhibiting SRGAP2A activity. 4) Inactivation of SRGAP2A is sensitive to the level of hetero-dimerization with SRGAP2C. 5) The primal form of SRGAP2C (P-SRGAP2C, existing between ∼3.4 and 2.4 Ma) is less effective in hetero-dimerizing with SRGAP2A than the modern SRGAP2C, which carries several substitutions (from ∼2.4 Ma). Thus, the genetic mutagenesis phase contributed to modulation of SRGAP2A's inhibition of neuronal expansion, by introducing and improving the formation of inactive SRGAP2A:SRGAP2C hetero-dimers, indicating a stepwise involvement of SRGAP2C in human evolutionary history.

Key words: **SRGAP2, X-ray crystallography, F-BAR domain, human evolution, structural biology.**

Introduction

Emergence of new genes is a powerful driving force of evolution and speciation. Gene duplication allows daughter copies to acquire function-altering mutations, without compromising the original activity of the mother gene. In recent years, comparing the modern human genome sequences to those of archaic hominins and great apes has allowed the discovery of duplicated genes unique to the *Homo* lineage. These genes are considered to have played key roles in human speciation, particularly in the development of the highly advanced human brain (Zhang and Long 2014; Dennis and Eichler 2016). One of these human-specific genes is *SRGAP2C*, which encodes for a functional protein, and originated from the ancestral *SRGAP2A* (fig. 1) (Sudmant et al. 2010; Dennis et al. 2012).

Slit-Robo GTPase Activating Protein (SRGAPs) couple the plasma membrane topology to remodeling of the actin cytoskeleton, thereby regulating neuronal migration, axon guidance and branching, and dendritic spine maturation. To achieve this task SRGAPs utilize a unique domain composition: an amino-terminal extended F-BAR (F-BARx), followed by RhoGAP and SH3 domains (fig. 1*B*), which mediate membrane association, cytoskeleton remodeling and protein–protein interactions, respectively. A model for the SRGAP2A mechanism of action can be deduced from recent (Fritz et al. 2015; Guez-Haddad et al. 2015) and previous studies (Wong et al. 2001; Pertz et al. 2008; Guerrier et al. 2009; Endris et al. 2011; Yamazaki et al. 2013) as well as from our current work. According to this model, SRGAP2A acts as an inhibitor of cell migration and protrusion extension. The activation of SRGAP2A begins with its recruitment to the vicinity of the plasma membrane by one of several target proteins (e.g. Robo1; Wong et al. 2001). Through its F-BARx domain, SRGAP2A directly binds to the plasma membrane, specifically at sites of protruding curvatures (Guerrier et al. 2009; Coutinho-Budd et al. 2012; Yamazaki et al. 2013). There, in an elegant example of negative feedback, the RhoGAP domain inactivates local pools of Rac1 and CDC42, which in turn, leads to the subsequent breakdown of nearby actin cytoskeleton, and the retraction of membrane protrusions (Wong et al. 2001; Fritz et al. 2015). SRGAP2C interacts with SRGAP2A and inhibits its activities (Charrier et al. 2012; Fossati et al. 2016). Expression of human SRGAP2C in cultured murine cortical neurons phenocopies SRGAP2A

Article

Open Access

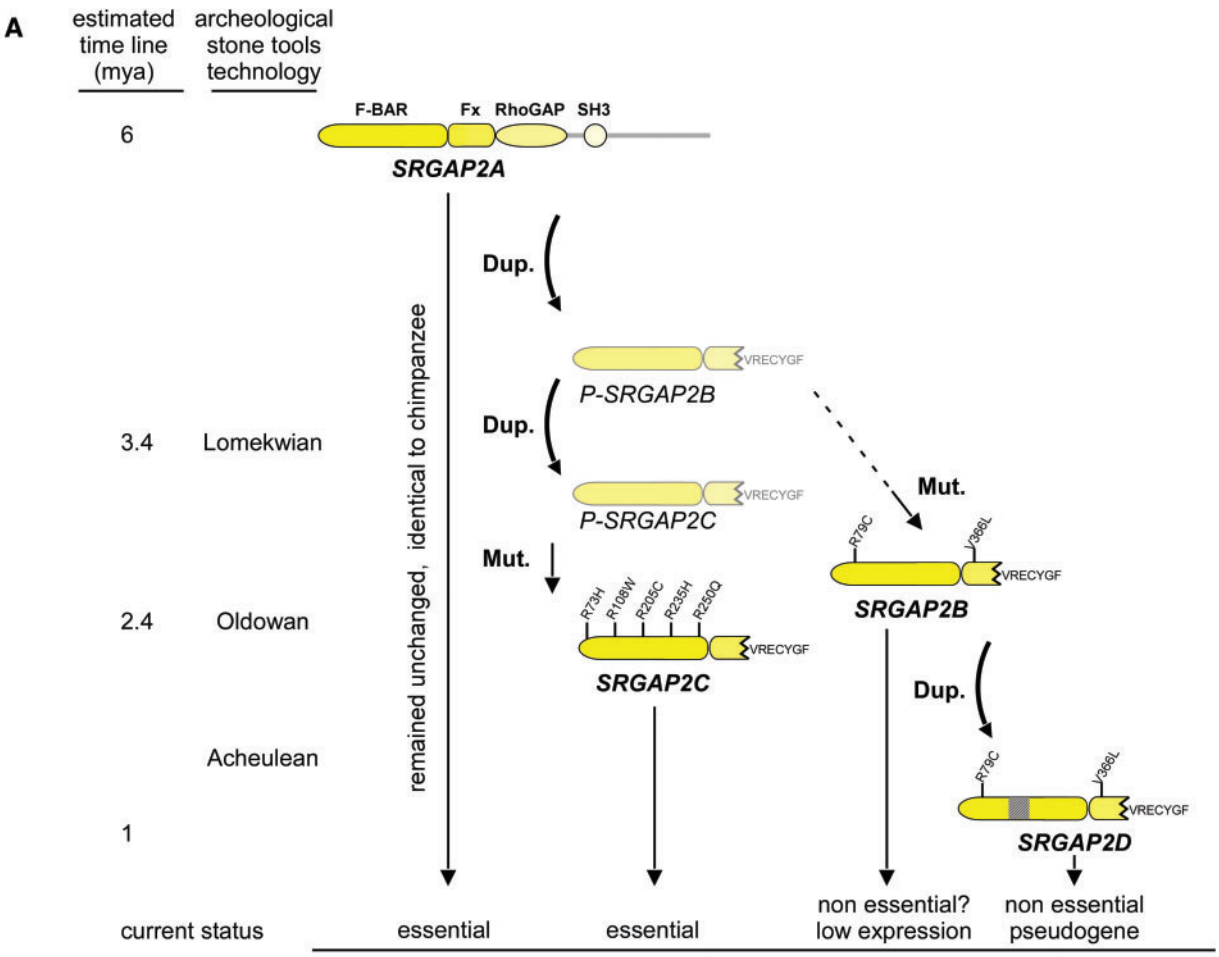

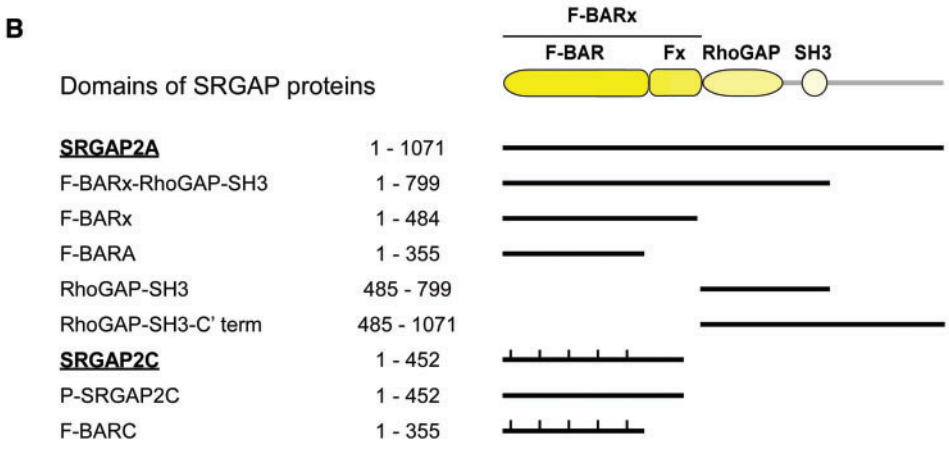

Fig. 1. Evolutionary history and domain organization of SRGAP2 proteins. (*A*) Evolutionary history diagram detailing the duplication (Dup.) and mutagenesis (Mut.) events in human *SRGAP2* genes and their current status in modern-day humans. A genetic approximate timeline and parallel stone tools technology archaeological dating (Harmand et al. 2015) shows correlation between the first and second mutagenesis events with the first and second generations of stone tools, ~3.3 and ~2.4 Ma, respectively. The missing carboxy-segment of the Fx in all the duplicated copies is indicated as a zig-zag tear followed by a seven-residue (VRECYGF) carboxy-terminal addition. Also indicated and detailed are the nonsynonymous mutations in the modern duplicated proteins. The primal forms of *SRGAP2B* and *SRGAP2C*, which existed prior to the accumulation of mutations are named with the prefix "*P-*." (*B*) Human SRGAP2A, SRGAP2C, and deletion mutants used in this study. In the scheme, the extended F-BAR (F-BARx) is subdivided into the F-BAR and the newly identified Fx domains. The RhoGAP and SH3 domains are also indicated and appear as yellow colored shapes. The five arginine alterations in the F-BAR domain of SRGAP2C are indicated by ticks.

knock down, resulting in an increased density of longer-necked dendritic spines (Charrier et al. 2012), a neuronal trait considered to be human-specific (Elston et al. 2001; Bianchi et al. 2013). It seems that like in many other cases, the inhibition (by SRGAP2C) of an inhibitor (SRGAP2A) drives evolutionary developmental processes (Gilbert and Barresi 2016).

SRGAP2C reached its current form after several evolutionary steps, determined by (Dennis et al. 2012) and are elaborated here in figure 1*A*. First, *SRGAP2A* underwent incomplete segmental duplication from chromosome 1q32.1 into 1q21.1, and then from 1q21.1 into 1p12. Later, nonsynonymous mutations accumulated on the duplicated copies: R79C and V366L on 1q21.1 giving rise to the contemporary *SRGAP2B*, and R73H, R108W, R205C, R235H, R250Q on the 1p12 copy, giving rise to the contemporary *SRGAP2C*. Here, we refer to the duplicated copies prior to the accumulation of the nonsynonymous mutations as "primal" or *P-SRGAP2B* and *P-SRGAP2C*. *SRGAP2B* was later duplicated once more into 1q21.1, to give rise to *SRGAP2D*. The emergence of *SRGAP2 B, C*, and *D* are estimated to have occurred ~3.4, ~2.4, and ~1 Ma, respectively.

The function of F-BAR (FES-CIP4 homology) domains, as well as those of the other members of the BAR superfamily [i.e., BAR (Bin/amphiphysin/RVS), I-BAR (inverse BAR), and N-BAR (N-terminal BAR) domains], is thought to be directly linked to their three-dimensional shape and oligomeric organization. BAR-superfamily domains form anti-parallel dimers that interact with membranes through their "N-surface", which is either concave, convex, or flat, and includes the amino-terminal helix ("helix 1") from the two anti-parallel BAR protomers. In this way, BAR, N-BAR, and certain F-BAR domains that have a concave N-surface associate with cellular membrane invaginations, while I-BARs that have convex N-surfaces associate with membrane protrusions. Consistent with their functions in endocytic processes, the crystal structures of membrane invagination-associating F-BAR family members, for example, FBP17, Syndapin, and FCHo2 (PDB codes 2EFL, 3HAH, and 2V0O, respectively), display a concave N-surface (Kessels and Qualmann 2015). It is therefore surprising to see that the endogenous SRGAP2A is localized to and active in cellular protrusions, such as dendritic spine heads and lamellipodia, and scaffold membrane protrusions, when overexpressed in COS-7 cells [(Guerrier et al. 2009; Charrier et al. 2012; Fritz et al. 2015) and this work].

Here, we show that dimeric SRGAP2A has an inverted, convex curvature that can promote membrane protrusions. We further show that SRGAP2A dimers exhibit a domain-swapping Fx coiled-coil extension domain, and that the RhoGAP-SH3 domains also participate in dimeric interactions. We found that in spite of its smaller size and reduced dimerization interface, SRGAP2C forms stable hetero-dimers with SRGAP2A, which are insoluble, cannot scaffold membranes, and have a reduced affinity for Robo1. We show that SRGAP2C acquired its full dominant negative function over time; while P-SRGAP2C was already insoluble due to a critical carboxy-truncation in the Fx, it was by the later mutagenesis stage that SRGAP2C gained its ability to form more stable SRGAP2A:SRGAP2C hetero-dimers.

Results

To reveal the molecular mechanism, by which SRGAP2A associates with membrane protrusions such as dendritic spine heads, and to understand how SRGAP2C inhibits SRGAP2A's activity during human brain development, we first determined the X-ray structure of the F-BARx, and used the resulting atomic coordinates to study the interplay between SRGAP2A and SRGAP2C. We docked the separate crystal structures of the F-BARx, RhoGAP (homology model), and SH3 domains into our previously determined SAXS structure of intact SRGAP4 (Guez-Haddad et al. 2015), and measured SRGAP2A inter-domain interactions to map the structural arrangement and dimeric interface within intact SRGAP2A homo-dimers. We employed liposome sedimentation assays to quantitate membrane binding affinity, single-turnover GTPase assay to measure GAP catalysis, and surface plasmon resonance (SPR) to measure SRGAP-Robo1 interactions. We used expression in Sf9 cells to evaluate protein solubility, and expression in COS-7 cells to assess the impact of SRGAP2A mutations on membrane-binding and remodeling activities, a method previously applied by other groups (Guerrier et al. 2009; Coutinho-Budd et al. 2012; Yamazaki et al. 2013).

F-BARx Crystallography

We solved the F-BARx crystal structure by applying a variation of an exhaustive molecular symmetry search approach that took advantage of the 2-fold anti-parallel F-BAR conserved symmetry (Sporny et al. 2016). This allowed solution of a structure (refined to 2.7 Å resolution) using a remote search model [FBP17, PDB 2EFL (Shimada et al. 2007)] with only 19% sequence identity, which represented 13% (as a poly-ala model) of the asymmetric unit contents. This molecular symmetry-constrained systematic search approach was vital for structure solution as it enabled the resolution of characteristic problems common for coiled coil proteins (Dauter 2015). The exhaustive search was followed by electron density modification procedures and cycles of model refinement and re-building (table 1). The quality of the resulting electron density has allowed us to ensure correct assignment of all amino acid side chains.

Crystal Structure of F-BARx

The crystal structure reveals that the F-BARx (residues 1–484, supplementary fig. S1, Supplementary Material online) is composed of a noncanonical F-BAR (residues 1–355) domain followed by a coiled-coil domain extension (residues 356–484), designated here as the F-BAR extension (Fx). The F-BARx is the largest BAR superfamily member characterized thus far. The tip-to-tip distance of the F-BARx dimer is approximately 275 Å [electron density in the tip regions is weak due to high B-factor values (supplementary fig. S2*B*, Supplementary Material online), and cannot be defined accurately], reaching a width of 55 Å. The buried surface interface (BSI) between the two protomers is 8370 $Å^2$. In comparison, the F-BAR domain of FBP17 has 288 residues, a dimeric tip-to-tip distance of 222 Å, a width of 36 Å, and a BSI of 4647 $Å^2$.

Regardless of the size difference, the same structural components that form the F-BAR domains of FBP17, CIP4, and FCHo2, are also found in SRGAP2A. These include three primary helices (α1, α2, and α3) and one short helix (α4) (fig. 2*A* and *B* and supplementary figs. S1 and S2, Supplementary

Table 1. Summary of Crystallographic Statistics.

Data Collection Statistics	
Crystal SRGAP2A F-BARx	
Beamline	ID-29 ESRF
Wavelength (Å)	0.976
Space group	C2
Unit Cell Parameters (Å)	a = 203.2, b = 29.9, c = 94.8, $\beta = 91.9^\circ$
Total reflections[a]	64,564 (2,660)
Unique reflections[a]	16,118 (726)
Completeness (%)[a]	98.8 (92.2)
R_{meas} (%)[a,b]	12.6 (121.1)
Mean I/σ[a]	8.1 (1.1)
Resolution range (Å)	47.36–2.70
CC1/2[a]	0.99 (0.62)
Refinement Statistics	
R_{work} (%)[a]	0.21 (0.38)
R_{free}(%)[a]	0.26 (0.40)
Number of nonhydrogen atoms	3386
Macromolecules	3367
Water	19
Protein residues	409
RMS bond lengths (Å)	0.013
RMS bond angles (°)	1.68
Ramachandran favored (%)	93
Ramachandran outliers (%)	0.2
Clashscore	2. 8
Average B-factor	80.05
RCBS PDB code	5I6J

[a]Values for the highest resolution shell are given in parentheses.
[b]$R_{meas} = \Sigma_h[m/(m-1)]^{1/2}\Sigma|_i I_{h,i} - < I_h > |/\Sigma_h\Sigma_i I_{h,i}$.

Material online). In SRGAP2A, the carboxy-half of α1 from each protomer, together with approximately one third of each α2 and α3, form a six-helix bundle at the center of the dimer, in which α1 and α3 are engaged in homotypic interactions with their dimeric counterpart.

Two arms protrude from the central helix bundle; each includes the long amino-half of α1, and a coiled-coil composed by the remaining two-thirds of α2 and α3.

The membrane-binding N-surface is composed by α1 and most of α2, together with small portions of α3 and α6. On the opposing side to the N-surface, the short α4 extends directly from α3 and further continues as a long random-coil towards the tip of the second protomer.

A Homer-EVH1 binding motif, ^{339}PPMKF, is located on the α4–α5 connecting loop (supplementary figs. S1 and S3, Supplementary Material online). It was recently demonstrated that through this motif, SRGAP2A directly interacts with the Homer protein in excitatory synapses (Fossati et al. 2016). However, our structural data reveals that because the Phe343 side-chain is buried in a cleft formed between the three main α1, 2, and 3 helices of the reciprocal protomer, it can actually not be engaged with EVH1 domain binding, unless a considerable conformational change takes place in this region. On the Homer side, this assessment is based on the crystal structure and analysis of the Homer EVH1 domain complexed with a peptide from mGluR (TPPSPF) (PDB 1DDV) (Beneken et al. 2000).

The Fx, a 72 Å long coiled-coil composed by α5 and α6, extends from one SRGAP2A protomer and packs against the α2–α3 arm of the reciprocal protomer in the SRGAP2A dimer (fig. 2 and supplementary fig. S2, Supplementary Material online). The Fx is arranged in such a way that α5 is predominantly surface exposed, and has only minor direct interactions with the F-BAR, while α6 is mostly buried between α5 and the α2–α3 coiled-coil arm. Similar coiled-coil extension with reminiscent packing is also observed in the crystal structure of the Fes-kinase F-BAR domain (PDB 4DYL).

SRGAP2A Has an Extended Dimerization Interface

Like other BAR-superfamily members, the isolated F-BAR domain (F-BARA, residues 1–355) of SRGAP2A is dimeric, as can be demonstrated by size-exclusion chromatography (SEC) (supplementary fig. S4, Supplementary Material online). The F-BARx crystal structure reveals an elaborated dimerization interface that involves the Fx in addition to the F-BAR.

Furthermore, we found that the RhoGAP-SH3 domains are also likely to be involved in dimerization (fig. 2C and D). With the F-BARx crystal structure at hand, we could fit it into the low resolution Small Angle X-ray Scattering (SAXS) structure of the full-length SRGAP4 that we determined recently (Guez-Haddad et al. 2015) (fig. 2D). Adjustment of the F-BARx arms angle by 10° and docking of RhoGAP (the homologous RhoGAP of Beta2-chimaerin, PDB 1XA6; Canagarajah et al. 2004) and SH3 (from our recent work, PDB 4RUG; Guez-Haddad et al. 2015) crystal structures into the densities next to the tips of the F-BARx arms results in a very good fit, using the fit-in-map application in Chimera (Yang et al. 2012), with real-time mean correlation = 9.0438e−05, SD = 0.00066913, RMS = 0.00067521. Domain fitting was also guided by distance constraints between the carboxy end of the Fx, which is visible in the crystal structure, and the amino terminus of the RhoGAP model. The resulting domain arrangement implies that the RhoGAP and SH3 domains interact directly with the F-BAR arms of the reciprocal protomers.

To confirm this observation, we measured the binding affinity of an isolated RhoGAP-SH3 to a fluorescently labeled F-BAR and F-BARx using microscale thermophoresis (MST) (fig. 2C). Our measurements show that the RhoGAP-SH3 domains specifically bind the F-BAR domain with $K_D = 3$ μM and the F-BARx with $K_D = 3.5$ μM. This shows that the RhoGAP-SH3 directly interacts with the F-BAR and that the Fx does not contribute to the binding affinity. These results are also consistent with our recent binding measurements of Robo1 to SRGAP2A (Guez-Haddad et al. 2015). Therein, we discovered that the F-BARx, RhoGAP, and SH3 domains cooperatively participate in Robo1 binding, further supporting direct interactions between the three domains.

In conclusion, the dimerization interface in SRGAP2A extends beyond the F-BARs, and includes the Fx and probably the RhoGAP-SH3 domains of one SRGAP2 protomer that wrap around the F-BAR domain of the reciprocal SRGAP2A (fig. 2D).

SRGAP2A Inverse Curvature

As mentioned earlier, it is typical for F-BAR proteins to associate with membrane invaginations, however, in concordance

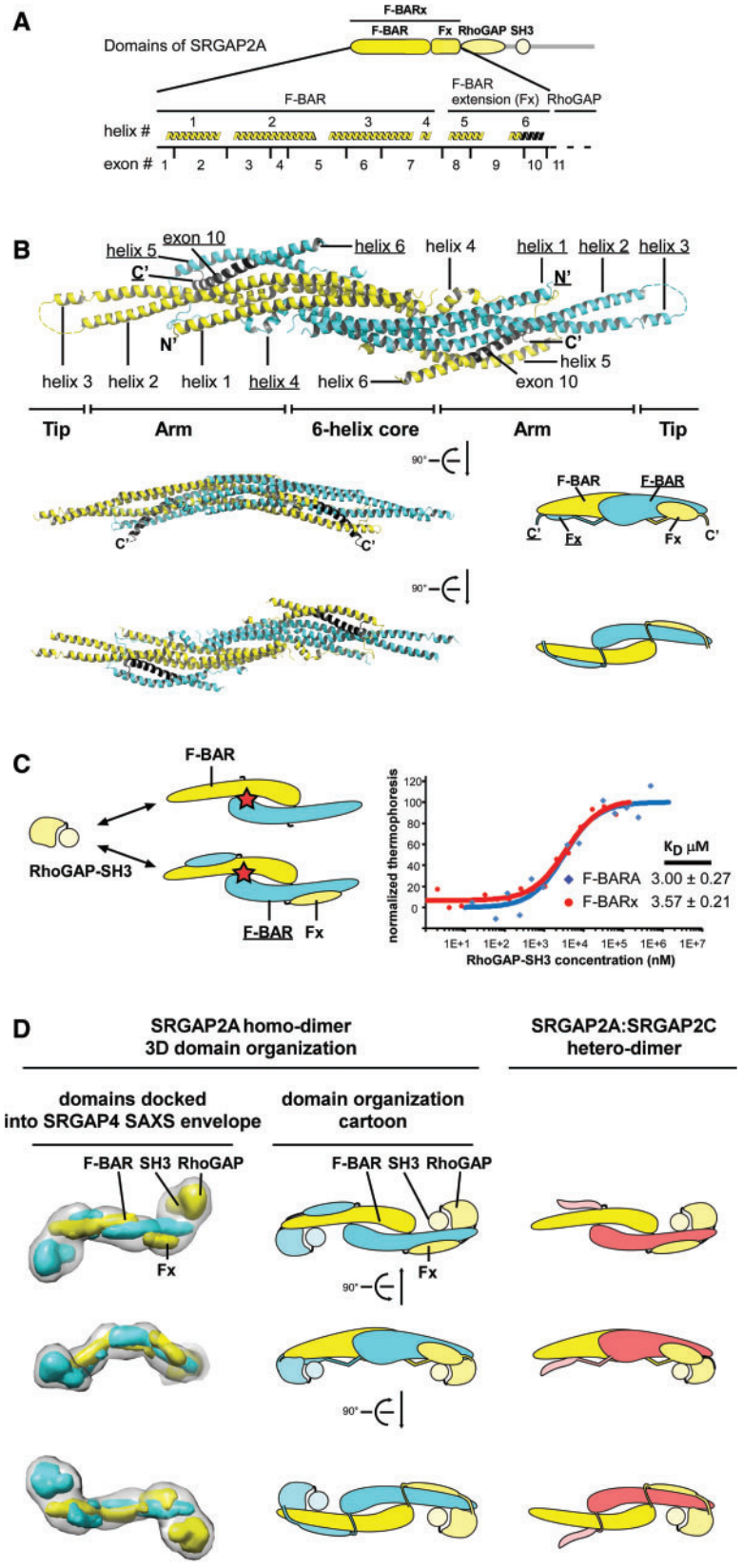

Fig. 2. SRGAP2A structure and dimerization. (*A*) Domains of SRGAP2A and focus on F-BARx. The F-BARx helices and encoding exons are drawn in scale and designated by their numbers. The carboxy-half of helix 6, encoded by exon 10, which is missing in SRGAP2C, is depicted in black. (*B*) Ribbon diagrams and cartoons of the dimeric SRGAP2A F-BARx crystal structure, in which the two identical protomers are colored in yellow and in cyan. Labels indicating structural elements of the cyan protomer are underscored. The large ribbon diagram represents a view facing the N-surface, and delineates the 6-helix core, arms, and tip regions. (*C*) The RhoGAP-SH3 domains bind directly to the F-BAR domain. Microscale thermophoresis (MST) titration curves and apparent K_D values for RhoGAP-SH3 binding to the F-BAR or the F-BARx that were fluorescently labeled. Measured

with prior studies, we find that the F-BAR-containing SRGAP2A associates with membrane protrusions (fig. 3B and C) (Frost et al. 2008; Guerrier et al. 2009; Yamazaki et al. 2013; Fritz et al. 2015). In order to explain how this might be, it is necessary to look at the structures of the SRGAP2A F-BAR domain in comparison to that of other F-BAR proteins. In general, the six-helix core region of F-BAR domains is essentially flat, and the overall curved shape of F-BAR dimers is generated by the direction and angle of the α2–α3 arms relative to the central region. In FBP17, CIP4, Syndapins, and FCHo2 the α2-α3 arms are bent towards the direction of the N-surface, thereby generating a concave membrane binding surface. Unlike these, our structural data for SRGAP2A reveal that the α2–α3 arms are bent in the opposite direction, away from the N-surface, resulting in a convex membrane binding surface (fig. 3A). Structure-based sequence comparison between the F-BAR domain of SRGAP2A and its closest available F-BAR homolog, FBP17 (PDB 2ELF, 19% sequence identity), revealed a 25-residue long helical insertion (residues ^{127}RFV. . .LQD^{151}) into α2 at the point that links the central region and the α2–α3 arm. Since the bases of the α2–α3 arms are held with α1 in the six-helix core region, the 25 aa insertion would push the α2–α3 arm to point away from the insertion. Indeed, when we removed the 25-residue helix from the F-BARx of SRGAP2A and expressed the truncated construct in COS-7 cells, no membrane protrusions were observed (supplementary fig. S5, Supplementary Material online). Taken together, such inverse geometry of the membrane-binding surface readily explains how, contrary to other F-BAR proteins, SRGAPs associate with membrane protrusions rather than with invaginations (fig. 3).

Membrane Binding Is Driven and Maintained by Electrostatic Interactions

In most BAR superfamily domains, membrane association is driven by electrostatic interactions between negatively charged membrane surfaces and positively charged residues on the membrane-binding surface of the protein (Mim and Unger 2012, Kessels and Qualmann 2015). For the SRGAP2A F-BARx, the convex N-surface is predominantly electropositive, while the opposite concave surface is electronegative (fig. 4A). We identified 46 lysine and arginine side chains that contribute to the electropositive potential of the dimeric N-surface (23 on each protomer). These positively charged residues are spread throughout the N-surface, with higher concentrations around the six-helix center and the two tip regions (fig. 4A and supplementary fig. S1, Supplementary Material online).

The Fx does not encroach upon the membrane-binding N-surface. In contrast, it constitutes a lateral addition that generates a transverse curvature, in addition to the more conspicuous longitudinal F-BARx curvature. To evaluate whether, and to what extent, the Fx contributes to membrane binding we compared liposome cosedimentation with F-BARA (residues 1–355, fig. 1B) to that of the F-BARx (residues 1–484). The results show that the presence of the Fx increases liposome binding by ∼25% (fig. 4B and supplementary fig. S6, Supplementary Material online). This result demonstrates that although the F-BAR is sufficient for membrane binding, the Fx strengthens membrane-association for SRGAP2A.

In order to experimentally test whether membrane binding is indeed mediated by electrostatic interactions, we first measured SRGAP2A F-BARx binding to liposomes under different conditions of phosphate concentration. In line with electrostatic interactions, binding was weaker as phosphate concentrations in the reaction buffer increased. About 140 mM phosphate almost completely dissociated F-BARx from liposomes after their prior association (fig. 4C). These experiments show that the F-BARx membrane association is primarily driven and maintained by electrostatic interactions. To confirm that the convex N-surface is the membrane-binding surface, we substituted five arginine and lysine residues with glutamates. The resulting RKKKR 54,55,234,235,238 EEEEE (designated F-BARx-R5E) contains charge alterations of three residues on each of the tips, and four in the six-helix center of the dimer (fig. 4A and supplementary fig. S1, Supplementary Material online). Liposome cosedimentation assays demonstrated that membrane binding of F-BARx-R5E was abolished (fig. 4B and supplementary fig. S6, Supplementary Material online), as was its ability to form membrane protrusions when expressed in COS-7 cells (fig. 4D).

Taken together, these experiments verify that the principle of membrane binding through the N-surface is retained in SRGAP2A, and demonstrate that membrane binding is a prerequisite for membrane scaffolding.

SRGAP2C Is Insoluble and Inflicts Insolubility on Coexpressed SRGAP2A

With the SRGAP2A F-BARx crystal structure at hand, we could readily investigate the molecular mechanism by which SRGAP2C antagonizes the activity of SRGAP2A.

SRGAP2C roughly spans the F-BARx of SRGAP2A, with three differences (fig. 1). First, SRGAP2C is missing exon 10 onwards. The F-BARx crystal structure now reveals that this leaves a carboxy truncation that disturbs the Fx fold. Second, it has a seven-residue (VRECYGF) carboxy-terminal addition, translated from intron 9. Third, it has five arginine alterations (R73H, R108W, R205C, R235H, and R250Q), all located on the F-BAR domain and none on the Fx. The first two

Fig. 2 Continued

thermophoresis values (symbols) fitted to a one-to-one binding model (solid lines). (*D*) 3D domain organization of SRGAP2A homo-dimers (left and center) and SRGAP2A:SRGAP2C hetero-dimers (right). SAXS 3D volume of full-length SRGAP4 (first shown in Guez-Haddad et al. [2015]) is represented as a transparent envelope into which the crystal structures of the F-BARx and the RhoGAP-SH3 domains were docked after being reduced to a 25 Å resolution 3D volumes by CHIMERA (Yang et al. 2012). SRGAP2C is colored in red and is missing the RhoGAP-SH3 domains as well as part of the Fx. Therefore, it forms an asymmetric hetero-dimer with SRGAP2A that has lesser dimeric interface than the SRGAP2A homo-dimer.

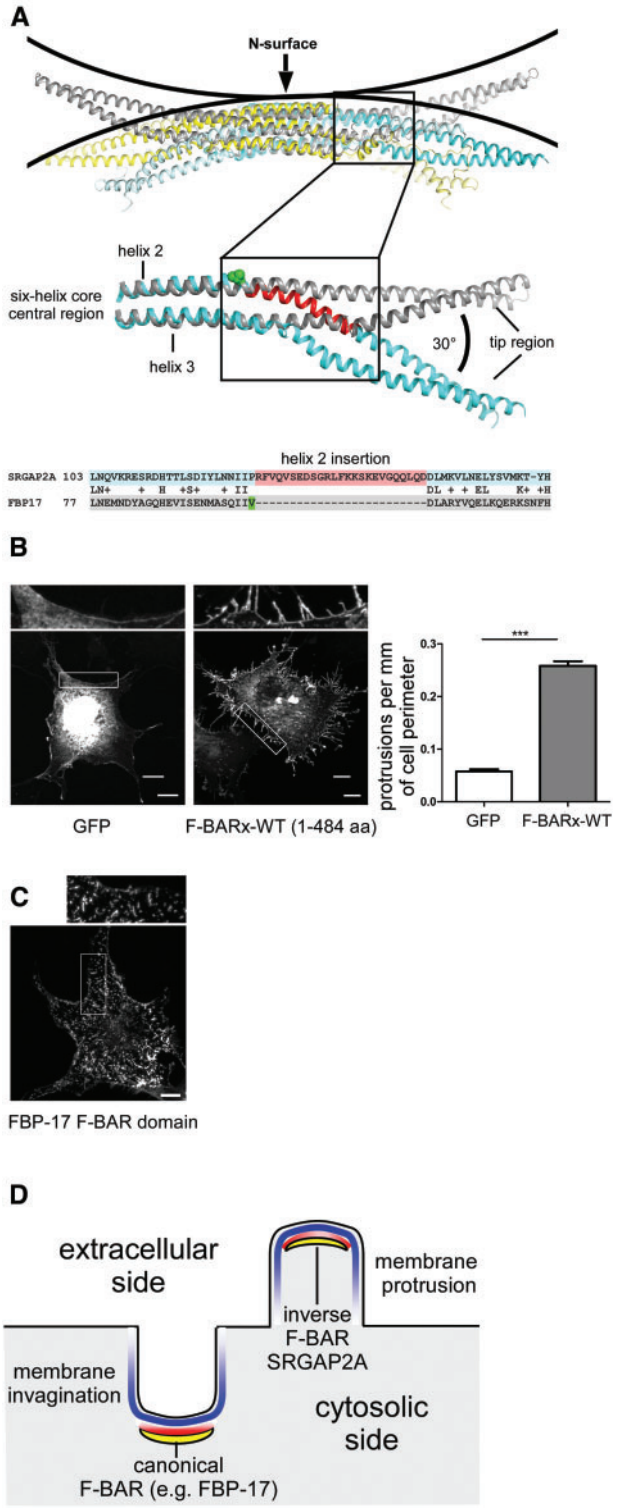

Fig. 3. An inverse F-BAR curvature in SRGAP2A. (*A*) The crystal structures of the SRGAP2A F-BARx homodimer (yellow and cyan) and the FBP17 F-BAR (PDB code 2EFL, both protomers colored in gray) are superimposed. While the six-helix core segments are well aligned, the arms of the SRGAP2A F-BARx point in opposite directions to those of the FBP17, thereby generating a convex N-surface. This view of the superimposed α2-α3 arms shows a ~30° inversion in the SRGAP2A F-BARx arm curvature. Colored in red is the 25 aa insertion segment in helix α2 that imposes the curvature inversion. Residue Val100 of FBP-17 is colored in green. (*B*) Maximum intensity projections of COS-7 cells transfected with GFP and GFP-fusion of the SRGAP2A F-BARx. Upper panel is a magnification of an area boxed in the image. Note that F-BARx-expressing cells are marked by high frequencies of protrusions from the plasma membrane. Bars, 10 μm. Quantitative determinations of protrusion frequencies at the perimeter of cells transfected as indicated. Data are mean + SEM. Statistical significances were tested using one-way ANOVA with Kruskal–Wallis and Dunn's post-tests. *$P < 0.05$; ***$P < 0.001$. (*C*) Maximum intensity projections of COS-7 cells transfected with GFP-fusion of the FBP17 F-BAR domain shows formation of membrane invaginations, a typical phenotype of canonical F-BAR domains. (*D*) While canonical F-BAR domains (e.g., FBP-17) that have a concave membrane binding surfaces associate with membrane invaginations and participate in endocytic processes, SRGAP proteins have an inverse, convex membrane binding surface that allows them to associate with membrane protrusions, for example, lamellipodia and dendritic spine heads.

modifications were inflicted simultaneously by the partial duplication of *SRGAP2A* (~3.4 Ma) (Dennis et al. 2012; Dennis and Eichler 2016) and were therefore present in the primal forms: *P-SRGAP2B* and *P-SRGAP2C* (fig. 1*A*). Because each of the contemporary forms (*SRGAP2B* and *SRGAP2C*) have different nonsynonymous substitutions, we conclude that all their substitutions (two on SRGAP2B and five on SRGAP2C) were introduced after *SRGAP2C* duplication from *SRGAP2B* (~2.4 Ma). As the contemporary F-BARx region in the human SRGAP2A sequence is 100% identical to those of chimpanzees (supplementary fig. S1, Supplementary Material online), bonobos and orangutans, we also conclude that SRGAP2A was unchanged at least in the past 6 My of human evolution (fig. 1*A*).

We first expressed SRGAP2C alone in COS-7 and Sf9 cells. SRGAP2C failed to induce membrane protrusions in COS-7 cells, displaying a granulated distribution in the cells' cytoplasm, and unlike SRGAP2A, was insoluble in the Sf9 culture (fig. 5*A–C*). We re-created P-SRGAP2C, which is an SRGAP2C that lacks the five arginine substitutions and is identical to P-SRGAP2B (fig. 1*B* and supplementary fig. S1, Supplementary Material online). P-SRGAP2C was also insoluble in Sf9 culture (fig. 5*D*). Consistently with our findings, Polleux and colleagues showed that an F-BARx that is missing exon 10, but lacks the five arginine substitutions does not generate membrane protrusions in COS-7 cells (Guerrier et al. 2009).

Analysis of the F-BARx crystal structure explains the reason for SRGAP2C and P-SRGAP2C insolubility. Since the part of helix 6 that is encoded by exon 10 supports the Fx structure, its absence in SRGAP2C (and P-SRGAP2C) would inflict Fx misfolding and insolubility due to exposure of significant hydrophobic patches (fig. 5*E*).

The insolubility of SRGAP2C and P-SRGAP2C is in sharp contrast to the full solubility of SRGAP2A (fig. 5). However, when coexpressed with either SRGAP2C or P-SRGAP2C, 60% and 40% of the SRGAP2A are found in the insoluble fraction, respectively (fig. 6*A–C*). It seems that SRGAP2C and P-SRGAP2C interact with SRGAP2A to pull it out of solubility.

We next investigated the properties of these interactions. Guided by the propencity of the SRGAP2A F-BAR domain to

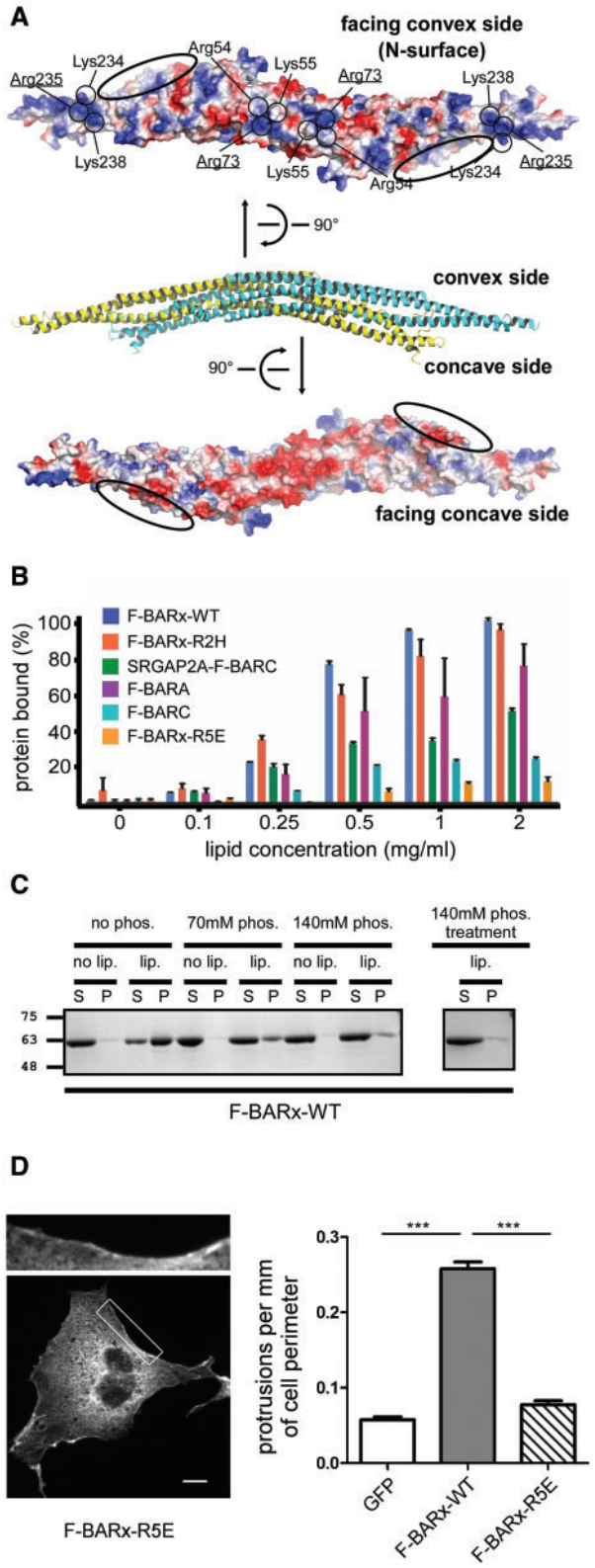

Fig. 4. SRGAP2A-membrane electrostatic interactions. (*A*) Electrostatic surface potential of F-BARx homodimer, projected onto its molecular surface using PyMOL (Schrödinger LLC). Note the contrast between the predominantly electropositive N-surface and the electronegative opposite surface. Key residues are indicated, and residues from one protomer are underlined while those of the second protomer are not. Fx regions are circled. (*B*) SRGAP2A F-BARx association with membranes is mediated by electrostatic interactions, as SRGAP2A F-BARx cosedimentation with liposomes is reduced by increasing concentrations of phosphate. Moreover, a pre-bound F-BARx is released by addition of phosphate (right panel). Supernatant (S) and pellet (P) fractions are indicated. (*C*) Gel densitometry quantification of liposome-bound fractions from cosedimentation experiments of SRGAP2A and SRGAP2C proteins, incubated with increasing concentrations of 400 nm sized liposomes composed from porcine whole brain extract lipids. The error bars indicate SEM; see supplementary figure S6, Supplementary Material online for SDS-PAGE Coomassie stained gels. (*D*) COS-7 cells expressing the F-BARx-R5E mutant show smooth surfaces, when compared with the F-BARx-WT in figure 3*B*. Quantitative protrusion analysis as in figure 3*B*.

form dimers, the underlying assumption is that native SRGAP2C protomers associate to form hetero-dimers with SRGAP2A protomers (Charrier et al. 2012; Dennis et al. 2012). Indeed, Polleux and coworkers coexpressed SRGAP2A and SRGAP2C in HEK293T cells and demonstrated that the two proteins interact, observed through coprecipitation (Charrier et al. 2012), suggesting direct interactions between the two proteins, but does not necessarily prove hetero-dimerization. Notably, the experiment by Charrier et al. does not contradict our finding that both SRGAP2C and the SRGAP2A:SRGAP2C complex are insoluble, since they used RIPA buffer containing denaturing ionic detergents (SDS and sodium-deoxycholate), capable of solubilizing the SRGAP2A:SRGAP2C complex.

The SRGAP2A:SRGAP2C Hetero-Dimerization Conundrum

Considering SRGAP2C's smaller dimeric contact interface and size (fig. 2*D*), the mechanism of hetero-dimerization that outcompetes the SRGAP2A homo-dimerization is not straightforward. We sought to investigate whether SRGAP2C interaction with SRGAP2A involves hetero-dimerization, and to further characterize the biochemical properties of SRGAP2C and the SRGAP2A:SRGAP2C complex. Because SRGAP2C and the complex that it forms with SRGAP2A are insoluble and therefore cannot be thoroughly investigated, we truncated the residual Fx of SRGAP2C, leaving a soluble F-BAR portion (residues 1–355, designated F-BARC, fig. 1*B*). This construct differs from its F-BARA counterpart by the five SRGAP2C arginine substitutions. We then coexpressed F-BARA and F-BARC (separately) with SRGAP2A (a construct spanning residues 1–799, the F-BARx-RhoGAP-SH3 domains, fig. 1*B*) in *E.coli*, and purified the SRGAP2A:F-BARA and SRGAP2A:F-BARC complexes using metal-chelate and size exclusion chromatography (supplementary fig. S7, Supplementary Material online). Strikingly, SEC-MALS (SEC in-line with multi-angle light scattering) analysis (fig. 6*D–F*) showed that while the SRGAP2A:F-BARA complexes tend to dissociate during elution (fig. 6*E*), F-BARC forms stable hetero-dimers with SRGAP2A (fig. 6*F*), that even withstand stringent ion exchange MonoQ chromatography conditions (supplementary fig. S7*E*, Supplementary Material online). Only coexpressed proteins form hetero-dimers, while proteins that were expressed and purified separately, could not exchange

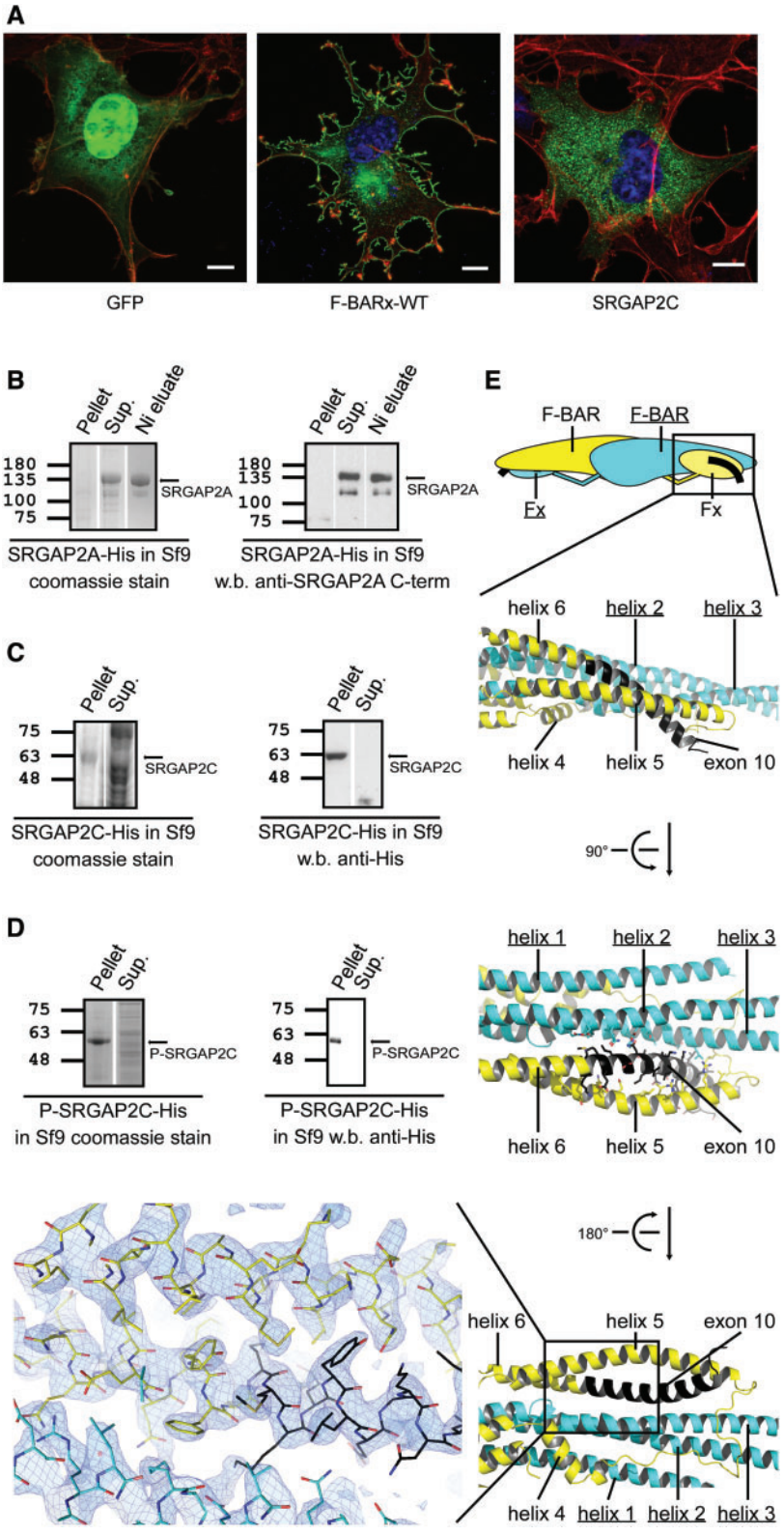

Fig. 5. SRGAP2C is insoluble due to Fx truncation. (*A*) GFP fusion of SRGAP2C expressed in COS-7 cells does not form membrane protrusions when compared with F-BARx, and shows a granulated cytosolic distribution. (*B*) When expressed alone in Sf9 cells, SRGAP2A is found exclusively in the soluble fraction. Coomassie-stained SDS-PAGE (left) and anti-SRGAP2A (abcam, ab124958 directed against the carboxy-tail of the protein that is not present in the SRGAP2C) western-blot analysis. SRGAP2A migrates next to the 135kDa marker. His-tagged SRGAP2A was expressed in Sf9 cells using the Bac-to-Bac system. P3 infected Sf9 cells (from one 2-l roller bottle, Greiner Bio-One) were harvested 72 h postinfection and lyzed in phosphate lysis buffer. The cell extract was centrifuged and the soluble fraction loaded onto a Ni-chelate column. Imidazole gradient was applied and the His-tagged SRGAP2A eluted at 100 mM imidazole. (*C* and *D*) His-tagged SRGAP2C (C) and His-tagged P-SRGAP2C (D) are found exclusively in the insoluble fraction. Both proteins were expressed as in (B) and analyzed using Coomassie-stained SDS-PAGE and anti-His

protomers when mixed, as evident from SEC analysis (supplementary fig. S7*F*, Supplementary Material online), indicating that pre-formed SRGAP2A homo-dimers dissociate very weakly, if at all.

These results are consistent with our observation that P-SRGAP2C (which does not have the five arginine substitutions, and is represented by F-BARA) is less effective than SRGAP2C (represented by F-BARC) in insolubilizing coexpressed SRGAP2A (fig. 6*A*–*C*).

In conclusion, the five arginine substitutions that were introduced to SRGAP2C in the later phase of its evolution facilitate tighter hetero-dimerization between F-BARC and SRGAP2A. In the case of the full-length SRGAP2C, these substitutions allow more effective insolubilization of coexpressed SRGAP2A.

SRGAP2C Substitutions Are Destabilizing, and Facilitate Tight Hetero-Dimerization

We considered three possible mechanisms by which the arginine substitutions of SRGAP2C may promote hetero-dimerization with SRGAP2A: (1) creation of new, direct interactions with SRGAP2A, (2) elimination of repulsive forces that may exist in an SRGAP2A homo-dimer, and (3) indirect effects.

Analysis of the F-BARx crystal structure does not support the possibility that the substitutions are engaged in new hetero-dimeric contacts with SRGAP2A. However, because we do not have an SRGAP2A:SRGAP2C crystal structure (the complex is insoluble) we cannot rule out this possibility. The second mechanism, that is, eliminating repulsive forces, appears more plausible. As homo-dimerization may involve overcoming same-charge repulsive forces, elimination of positive charges (interestingly, all five substitutions are of arginine residues) from SRGAP2C would promote hetero-dimerization. The third possibility, indirect effects, concerns altered structural properties of SRGAP2C itself. To investigate the structural changes that the arginine substitutions may inflict, we compared the observed solubilities and stabilities of F-BARC and F-BARA after expressing them individually in *E. coli* (fig. 7*A* and *B*). While F-BARA is mostly found in the soluble fraction, F-BARC is mostly (but not entirely) insoluble. Nevertheless, once isolated to homogeneity, F-BARA and F-BARC show similar SEC elution and CD spectra profiles (supplementary fig. S4, Supplementary Material online and fig. 7*C*, respectively), demonstrating that both have the same general fold and dimeric arrangement.

We next measured the thermal stability of purified F-BARC and F-BARA and found that they have profoundly different denaturation profiles (fig. 7*D*). The F-BARC denaturation slope is wider and is considerably less thermo-stable than F-BARA, with denaturation temperature values of 32 and 38 °C, respectively (fig. 7*E*). The wider denaturation slope of F-BARC demonstrate a loss of cooperativity in the F-BARC structure (Kuwajima 1989), in which the F-BARC retains an F-BARA-like fold, but with a looser packing of the three long helices in the tertiary structure.

We next introduced each one of the five arginine substitutions separately into F-BARA, and found that the greatest destabilization effect is inflicted by the R108W mutation (fig. 7*F*). We next showed that R108K, R108L, and R108S substitutions did not have the same effect, which implies that the destabilizing effect of R108W is due not only to loss of arginine interactions, but is rather inflicted by a tryptophan-specific contribution (supplementary fig. S8, Supplementary Material online).

Taken together, these results reveal a fundamental biochemical property of SRGAP2C: structural instability of the F-BAR fold. This property was acquired at the final stage of SRGAP2C evolution, with the mutagenesis of R108 to tryptophan, and is not present in P-SRGAP2B and P-SRGAP2C.

SRGAP2A:F-BARC Hetero-Dimers Are Also Defective in Membrane Binding and Robo1 Association, but Not in RhoGAP Activity

Up to this point, we showed that SRGAP2C hetero-dimerizes with SRGAP2A, and that once formed, these hetero-dimers do not dissociate and are insoluble, which explains SRGAP2A inactivation by SRGAP2C. Next, we investigated whether additional properties of SRGAP2A (critical for its cell biological functions) are modulated by hetero-dimer formation with SRGAP2C. Since SRGAP2C and SRGAP2A:SRGAP2C hetero-dimers are insoluble, and cannot be isolated for biochemical investigations, SRGAP2A:F-BARC heterodimers were used for measurements of membrane binding and scaffolding, RhoGAP catalysis activity and Robo1-CC3 binding, as these are soluble.

Liposome cosedimentation experiments showed that F-BARC and SRGAP2A:F-BARC hetero-dimers have a reduced affinity for membranes in comparison to F-BARA, F-BARx, and SRGAP2A (fig. 4*B* and supplementary fig. S6, Supplementary Material online). In addition, while F-BARA shows some membrane scaffolding activity in COS-7 cells, F-BARC does not (supplementary fig. S9*A*, Supplementary Material online).

We considered that the SRGAP2C arginine substitutions, in particular those engaged in direct electrostatic contacts with the negatively charged membrane, inflict weaker SRGAP2C membrane binding. Mapping the five substituted arginine residues of SRGAP2C onto the F-BARx crystal structure (supplementary fig. S10, Supplementary Material online) reveals that two of them: R73 and R235 point at the membrane binding surface. The third arginine residue (R250) is positioned on the opposite surface, the fourth (R108) is packed against the molecule's side, and the fifth (R205) is located at the arm tip region, where electron density is not

Fig. 5 Continued

western-blot analysis. Both SRGAP2C and P-SRGAP2C migrates below the 63 kDa marker. (*E*) Cartoon, ribbon, and electron density map representation of the missing-in-SRGAP2C exon 10 structure. Exon 10 encodes for the carboxy-half of helix α6 that mediates the Fx interactions with the F-BAR α2–α3 arm and is thereby essential for the Fx fold integrity. In its absence, the amino-half of helix α6 and the entire α5 helix loses their hold on the F-BAR arm and the structural integrity of the Fx. Fx misfolding due to the missing exon 10 readily explains SRGAP2C and P-SRGAP2C insolubility. A simulated annealing composite omit electron density map contoured to 1.3σ, highlighting the close contacts of helix 6 with helix 5 of the Fx, and with the F-BAR portion of the reciprocal F-BAR protomer.

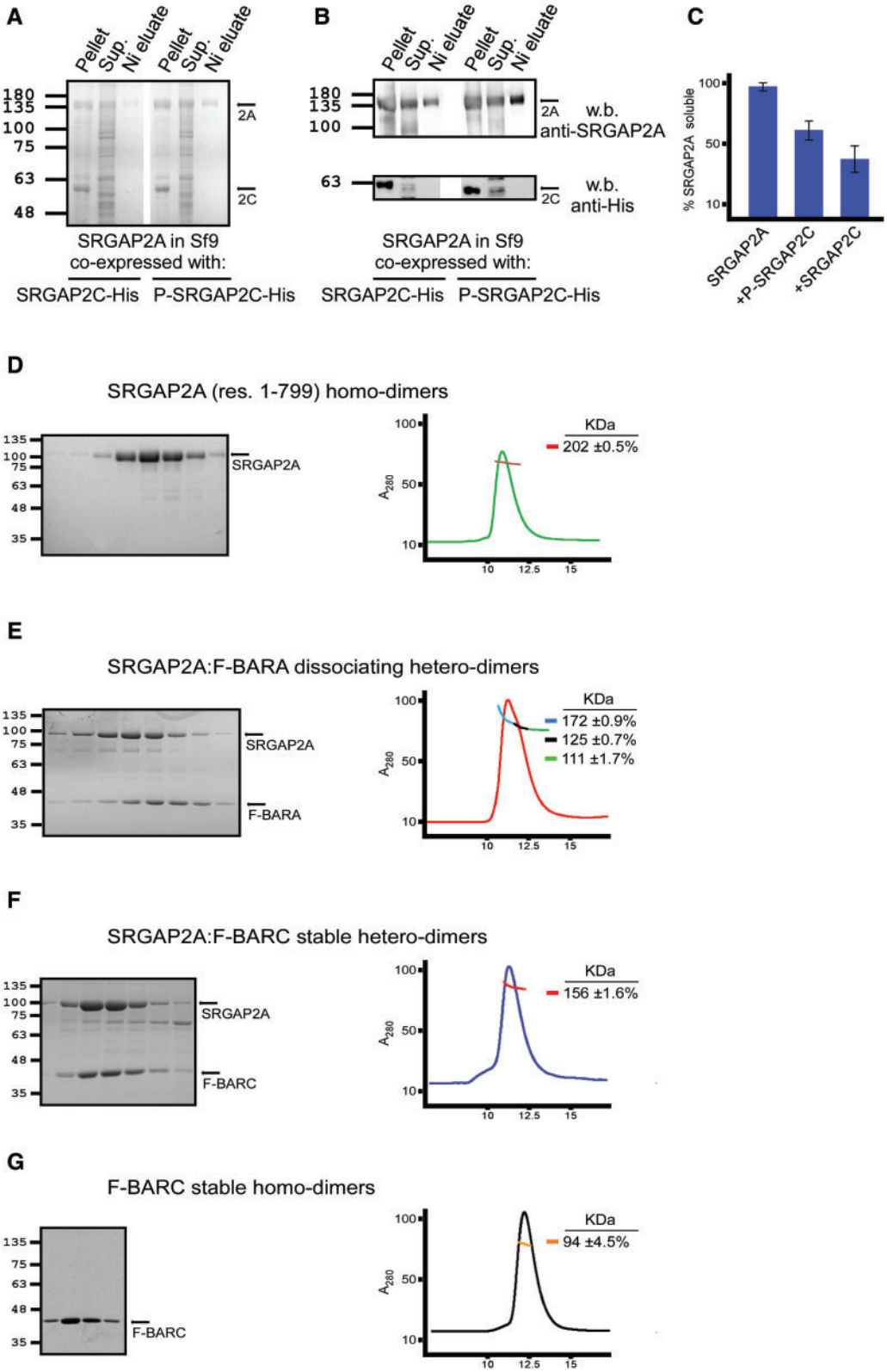

Fig. 6. SRGAP2A:SRGAP2C hetero-dimerization. (*A*–*C*) Coomassie-stained SDS-PAGE (A) and western-blot analysis (B) show that, in sharp contrast to SRGAP2A solubility (fig. 5*B*), large amounts of (nontagged) SRGAP2A are in the insoluble fraction when coexpressed with either His-tagged SRGAP2C or His-tagged P-SRGAP2C in Sf9 cells. Important to note that the nonHis-tagged SRGAP2A binds to the Ni-chelate column and elutes at 50 mM imidazole. SRGAP2C and P-SRGAP2C remain insoluble under coexpression conditions. (*C*) Gel densitometry quantification of SRGAP2A soluble fraction (calculated from [*A*] and fig. 5*B*), as the ratio between the total amount of protein in the Ni-column elution and the insoluble fraction. The error bars indicate SEM. (*D*–*F*) Coomassie stained SDS-PAGE of superose6 10/300 elution profiles, and SEC-MALS analysis of SRGAP2A (residues 1–799, F-BARx-RhoGAP-SH3) alone (*D*), coexpressed with F-BARA (SRGAP2A residues 1–355) (*E*), or coexpressed with F-BARC (SRGAP2C residues 1–355) (*F*). Note that while the SRGAP2A:F-BARA complex dissociates into a homo- and hetero-dimers mixture under

clearly visible. The SRGAP2C substitutions R73H and R235H deprive the membrane binding surface of two of its positive charges, and are therefore likely to reduce the protein's affinity for negatively charged membranes. We introduced SRGAP2C's R73H and R235H substitutions to the F-BARx construct (termed F-BARx-R2H) and compared the mutant's membrane binding to that of F-BARx-WT. F-BARx-R2H showed mildly reduced binding to liposomes (fig. 4*B* and supplementary fig. S6, Supplementary Material online) and reduced protrusion formation in COS-7 cells (supplementary fig. S9*B*, Supplementary Material online).

We next measured and compared the binding affinity of Robo1 for SRGAP2A and the SRGAP2:F-BARC hetero-dimer. Previously, we have found that the SRGAP2A SH3 domain is necessary, but not sufficient for an effective Robo1–SRGAP2A interaction, and that the addition of the RhoGAP and F-BARx domains change the binding kinetics and greatly strengthen Robo1–SRGAP2A association (Guez-Haddad et al. 2015). Specifically, measured K_D values for Robo1–CC3 association with SH3, RhoGAP–SH3, and F-BARx–RhoGAP–SH3 were 13, 4.5, and 0.6 μM, respectively. We concluded that the F-BARx, RhoGAP, and SH3 domains form a composite surface that binds the Robo1-CC3 better than the isolated SH3 domain. Surface plasmon resonance (SPR) studies of the SRGAP2A:F-BARC hetero-dimer interactions with Robo1-CC3, revealed a kinetic profile significantly different to that of SRGAP2A. The Robo1 interaction was significantly weaker and the obtained kinetic profile merely reached that of a RhoGAP-SH3 fragment, with a calculated K_D value of 5.6 μM (supplementary fig. S11*A*, Supplementary Material online). These results indicate that the composite F-BARx–RhoGAP–SH3 Robo1 binding surface in the SRGAP2A:SRGAP2C hetero-dimer is disturbed, thus hampering potential to be recruited to Robo1 signaling sites.

In contrast, the enzymatic GAP activity (Rac1 GTP hydrolysis rate, evaluated using the single-turnover GTPase assay) of an isolated SRGAP2A RhoGAP domain was similar to that of SRGAP2A:F-BARC hetero-dimers (supplementary fig. S11*B*, Supplementary Material online).

Taken together, these experiments show that arginine substitutions in SRGAP2C reduce its affinity for negatively charged membranes, and that a soluble truncation of SRGAP2C (F-BARC) is incapable of membrane scaffolding in COS7 cells. A soluble version of the SRGAP2A:SRGAP2C hetero-dimer (SRGAP2A:F-BARC) also shows weaker affinity for membranes. Furthermore, this SRGAP2A:F-BARC hetero-dimer has a weaker affinity for Robo1, which reflects a defective F-BARx–RhoGAP–SH3 domain arrangement, disturbing the ligand-binding mechanism, and thereby effectively antagonizing SRGAP2A functions.

Discussion and Conclusions

In 2012, Polleux and colleagues (Charrier et al. 2012) showed that SRGAP2C ectopic expression in cultured mouse neurons has a similar effect to SRGAP2A knock down, suggesting that this antagonizing function played a key role in the development of unique features of the human brain. In this work, we present and analyze the structure of SRGAP2A, the interplay between SRGAP2A with the human specific paralog SRGAP2C, and unveil a molecular mechanism by which the human specific SRGAP2C progressively acquired the ability to antagonize SRGAP2A.

A New BAR Domain Fold

Our work reveals a new BAR domain fold: the "inverse F-BAR", which explains how SRGAP2A interacts with membranes in protruding sub-cellular regions as opposed to invaginated endocytic sites, the typical interaction for canonical F-BAR proteins (fig. 3).

The crystal structure of the extended F-BAR domain (F-BARx) of SRGAP2A also reveals domain-swapped coiled-coil F-BAR extensions (Fx) that pack on the lateral sides of the reciprocal F-BAR protomers. Direct MST binding measurements and fitting of crystal structures into the 3D SAXS envelope of full-length SRGAP4 shows that the RhoGAP-SH3 domains are also likely to participate in dimeric interactions, revealing a large SRGAP2A dimerization interface that includes the F-BAR, Fx, and RhoGAP-SH3 domains (fig. 2).

SRGAP2C Hetero-Dimerization with and Inactivation of SRGAP2A

We show that the antagonism of SRGAP2A by SRGAP2C has two separate, yet equally imperative components. One is the hetero-dimerization of the two proteins, and the second is the inactivation of the hetero-dimerized SRGAP2A.

We demonstrate that unlike the soluble SRGAP2A, SRGAP2C is insoluble and that consequently, SRGAP2A:SRGAP2C hetero-dimers are also insoluble. SRGAP2C's insolubility is inflicted by a carboxy-truncation in the Fx that most likely results in Fx misfolding. As an insoluble complex, SRGAP2A:SRGAP2C hetero-dimers aggregate, unable to reach designated recruitment sites, an impediment that by itself renders the SRGAP2A:SRGAP2C complex inactive. Nonetheless, by engineering a soluble version of SRGAP2C (F-BARC) we could, to some extent, probe the biochemical properties of the SRGAP2A:F-BARC hetero-dimers and show that these hetero-dimers are additionally impaired in other aspects besides solubility: they have weaker membrane- and Robo1-binding affinities.

SRGAP2A–SRGAP2C hetero-dimerization poses a thermodynamic puzzle. Evidence for the contribution of the Fx and RhoGAP–SH3 domains to dimerization, raises the question of how does SRGAP2C, that lacks the RhoGAP–SH3 domains and has an impaired Fx, form hetero-dimers while competing with the larger and seemingly favorable SRGAP2A homo-dimers? We show that unlike the stable SRGAP2A:F-BARC hetero-dimers, dimers between SRGAP2A and F-BARA are

Fig. 6 Continued
gel-filtration conditions, the SRGAP2A:F-BARC hetero-dimers are remarkably stable. An elaborate description of the SRGAP2A:F-BARC and SRGAP2A:F-BARA hetero-dimers production is presented in supplementary figure S7, Supplementary Material online. (*G*) Coomassie stained SDS-PAGE of superose6 10/300 elution profiles, and SEC-MALS analysis of F-BARC.

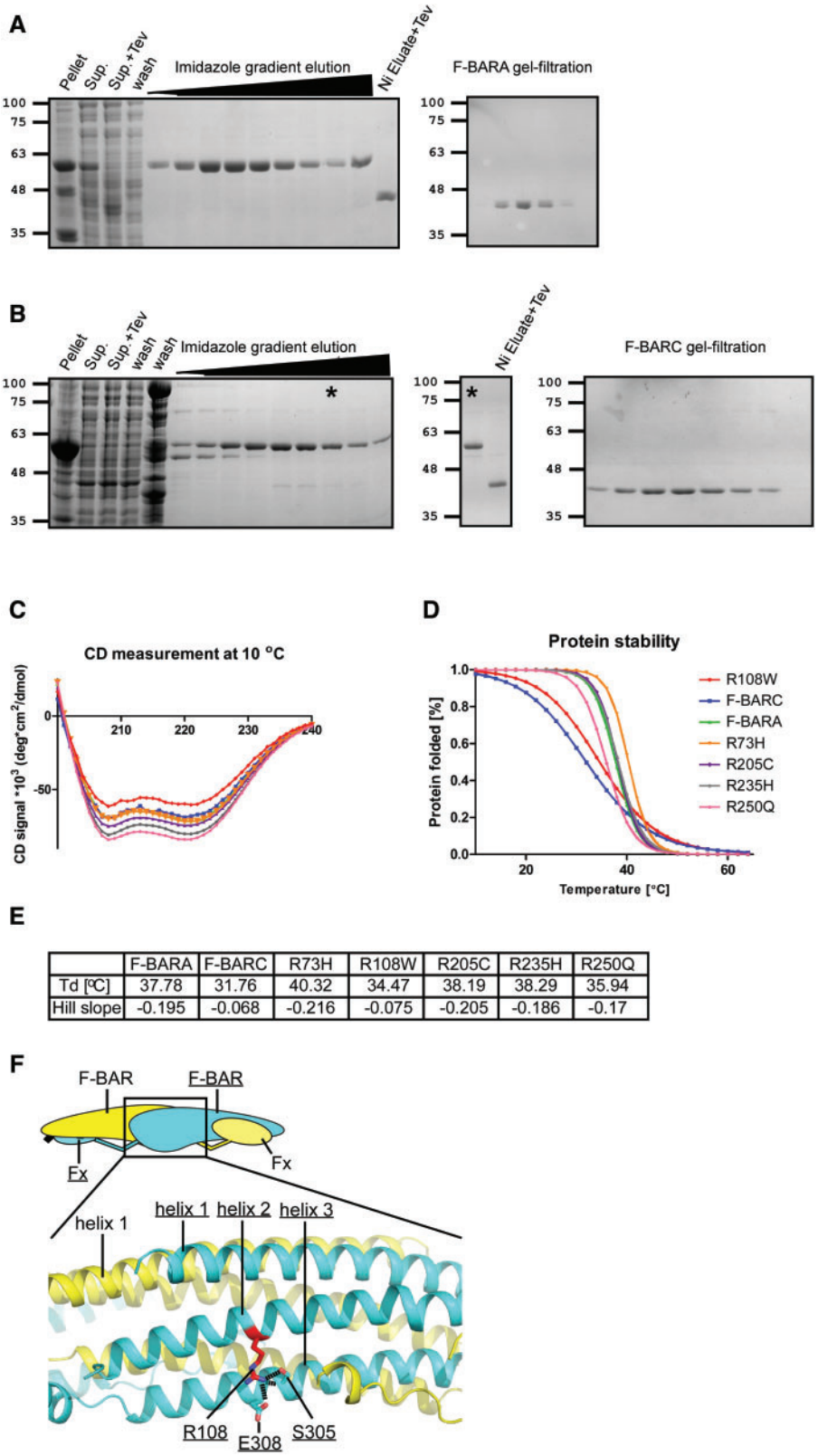

	F-BARA	F-BARC	R73H	R108W	R205C	R235H	R250Q
Td [ºC]	37.78	31.76	40.32	34.47	38.19	38.29	35.94
Hill slope	-0.195	-0.068	-0.216	-0.075	-0.205	-0.186	-0.17

Fig. 7. The SRGAP2C R108W substitution inflicts structural instability. F-BARA (*A*) and F-BARC (*B*) were expressed as -TEV-His-Trx fusions in *E. coli*. The proteins were eluted by an imidazole gradient from Ni-NTA column, digested by TEV protease, and further purified by a superdex200 20/60 gel filtration column. (*C*) The purified F-BARA and F-BARC, as well as each one of the SRGAP2C point mutants introduced to the F-BARA template (which were expressed and purified like F-BARA and F-BARC) were analyzed by circular dichroism (CD) spectroscopy in 10 °C. All seven F-BAR constructs show similar CD spectra, with a predominantly alpha helical secondary structure content. (*D*) Temperature gradient CD analysis (average of three runs) shows a reduced thermal stability and structural cooperativity of F-BARC and the R108W mutant in comparison to F-BARA. (*E*) Calculated denaturation temperatures (T_d) and denaturation slopes are presented for each F-BAR construct. (*F*) Zoom in on the R108 region and interactions.

not stable and dissociate into separate SRGAP2A and F-BARA populations during SEC elution (fig. 6 and supplementary fig. S7, Supplementary Material online). Evidently, F-BARC and F-BARA behave very differently in respect to association with SRGAP2A. We found that this difference stems from the five arginine substitutions present in SRGAP2C. R108W, which has a dramatic effect on the thermal stability of the F-BAR in SRGAP2C, causes loosening of structural cooperativity and a decrease in the denaturation temperature of the F-BAR (fig. 7). We suggest that the stabilization of SRGAP2C in the SRGAP2A:SRGAP2C hetero-dimers brings a thermodynamic gain that allows SRGAP2C, despite its smaller dimerization surface, to compete with thermodynamically favorable SRGAP2A homo-dimerization.

Were the Primal P-SRGAP2B/P-SRGAP2C Biochemically Different to Modern SRGAP2C, and If So, How?

The five arginine substitutions in modern SRGAP2C (including R108W) were acquired in the final stage of SRGAP2C evolution (fig. 1). Thus, we propose that the primal forms of SRGAP2C, if they were indeed active during the period of their existence, were less effective in SRGAP2A hetero-dimerization and therefore in antagonizing SRGAP2A functions.

Throughout an estimated 1 My (~3.4–2.4 Ma), *SRGAP2B* and *SRGAP2C* existed in their primal forms. The amino acid sequences of these partially duplicated *SRGAP2A* copies were identical to each other, free from nonsynonymous substitutions (fig. 1A). Later, each acquired a different set of non-synonymous mutations, giving rise to the modern forms: *SRGAP2B* and *SRGAP2C* (Dennis et al. 2012). An interesting question is whether the primal copies differed from the modern ones. In this work, we show that the biochemical properties of P-SRGAP2B/P-SRGAP2C were different from those of modern SRGAP2C. Although both SRGAP2C and P-SRGAP2B/P-SRGAP2C appear insoluble on isolation, the primal forms are less effective in bringing coexpressed SRGAP2A out of solubility (fig. 6A–C). As a result, more SRGAP2A homo-dimers were able to form and signal effectively, while presence of coexpressed modern SRGAP2C brought about stronger attenuation of SRGAP2A functions.

The final question is: could it be possible that SRGAP2C mutants designed to make stronger heterodimeric contacts with SRGAP2A, would further attenuate activity, and what might be the physiological effects of this.

Experimental

Design and Cloning of SRGAP Constructs

The human SRGAP2A full-length cDNA clone (KIAA0456) was purchased from ImaGenes GmbH, and its internal BamHI digestion site was mutated by polymerase cycling assembly. SRGAP2C was cloned from a human cDNA library, and P-SRGAP2C was prepared using the SRGAP2A cDNA template for PCR amplification (SRGAP2A 1–452) with reverse primer that adds the carboxy-extension ^{453}VRECYGF^{459} (primal sequences derived from Dennis et al. 2012).

Mutants were generated by PCR with appropriate primers introducing the mutations. Multiple mutations were introduced by multiple rounds of mutagenesis using templates already carrying some of the desired mutations. All constructs generated by PCR were checked by sequencing.

For *E. coli* expression, SRGAP2 constructs were digested with BamHI and XhoI and ligated into a modified pHis-parallel2 vector (Novagen), with an amino-terminal His-Tag, TRX fusion protein, and TEV cleavage sequence. The RhoGAP-SH3-C' term (SRGAP2A 485–1071) construct was digested with BamHI and XhoI and ligated into a His-tag deleted pET28 vector (Novagen). The F-BARx–RhoGAP–SH3 (SRGAP2A 1–799) construct was digested with BamHI and NotI and ligated into a modified pRSFDuet-1 vector (Novagen), with the N-terminal His-tag replaced by a SUMO fusion protein.

For Sf9 expression, full length SRGAP2A, SRGAP2C, and P-SRGAP2C cDNA was digested with BamHI and XhoI and ligated into the pFastBac-HTB vector (Invitrogen) with a carboxy-terminal His–Tag. The pFastBac Dual vector (Invitrogen) was used to coexpress SRGAP2A (no tag, ligated at the EcoRI and SalI sites) under the polyhedrin promoter, with either SRGAP2C or P-SRGAP2C (both His-Tagged, ligated at the XhoI and NheI sites) under the p10 promoter.

For COS-7 expression, SRGAP2constructs were GFP-fusions encoded by pEGFP.

Expression and Purification

For bacterial expression, all constructs were expressed in *E. coli* BL21 Tuner strain (Novagen), also expressing the RIL Codon Plus plasmid (Barak and Opatowsky 2013). Transformed cells were grown for 3–4 h at 37 °C in 2xYT media containing 100 μg/mL ampicillin and 34–50 μg/mL chloramphenicol. Protein expression was induced with 200 μM IPTG over a 16 h period at 16 °C. Cells were harvested and frozen prior to lysis and centrifugation. For *in vitro* assays, F-BARx-RhoGAP-SH3, F-BARx, F-BARA, F-BARC, and coexpressed protein constructs were purified by the following steps: supernatant was loaded onto a pre-equilibrated Ni-chelate column (HisTrap, GE Healthcare) with buffer A [50 mM Phosphate buffer, pH 8, 400 mM NaCl, 5% glycerol, 5 mM β-MercaptoEthanol (βME)], washed and eluted with a buffer B gradient (50 mM Phosphate buffer, pH 8, 400 mM NaCl, 5% glycerol, 500 mM imidazole, 5 mM βME). Protein-containing fractions were pooled, incubated with TEV protease (1:50 v/v) and dialyzed O/N at 4 °C against buffer A. The protein was then passed through a Ni-chelate column and further isolated by SEC (HiLoad 26/60 Superdex 200 column, GE Healthcare), pre-equilibrated with buffer C (120 mM NaCl, 50 mM phosphate buffer pH 8, 1 mM DTT). Proteins were concentrated using Vivaspin 20 (Sartorius). When required, SUMO and TRX fusions were removed by TEV and/or SENP proteolysis. For quality control, purified proteins were analyzed by SEC and circular dichroism.

Baculoviruses ware generated using the Bac-to-Bac® system (Invitrogen). Proteins were expressed in baculovirus-infected Sf9 cells grown in 50ml ESF 921 culture medium (Expression systems) using a 2 L roller bottle (Greiner Bio-One). P3 infected

Sf9 cells were grown at 27 °C and harvested after 72 h by centrifugation (200 × g, 10 min), then frozen in liquid N_2. Cell pellets were thawed and re-suspended in 10 ml buffer D (50 mM Phosphate buffer, pH 7.5, 200 mM NaCl, 5 mM βME, 5% glycerol (w/v), 0.5 mM EDTA). About 2 mM PMSF was added after lysis using a dounce homogenizer. Cell lysates were clarified by centrifugation at 20,000 × g for 20 min and the supernatant treated as above for Ni-chelate column purification using buffer D for equilibration and buffer E for a gradient elution [50 mM Phosphate buffer, pH 7.5, 200 mM NaCl, 5 mM βME, 5% glycerol (w/v), 0.5M imidazole]. Eluted fractions were analyzed by SDS-PAGE and immunoblotting with anti-His (Santa Cruz) and anti-SRGAP2A (abcam, ab124958) antibodies.

Cell Culture, Transfection, and Staining

HEK293 cells and COS-7 cells were maintained in 10 ml DMEM containing 2 mM L-glutamine, 10% (v/v) fetal bovine serum and gentamycin at 37 °C and 5% CO_2.

HEK293 cells were seeded in six-well plates and transfected with TurboFect according to manufacturer's instructions (Thermo Scientific) 12 h later. Twenty-four hours after transfection, cells were harvested, resuspended in homogenization buffer [5 mM HEPES pH7.4, 0.32 M sucrose, 1 mM EDTA supplemented with Complete® protease inhibitor (Roche)], and homogenized by passing through a syringe and pottering (12 strokes). The lysates were centrifuged for 10 min at 1000 × g at 4 °C to remove cell debris and nuclei. The supernatant was then spun at 11,700 × g for 20 min at 4 °C to obtain a crude membrane fraction. The membrane fraction was then resuspended in homogenization buffer and again spun to yield a washed membrane fraction as a pellet. Aliquots were analyzed by anti-GFP immunoblotting.

COS-7 cells were seeded in 24-well plates and transfected ~8 h later using TurboFect (Thermo Scientific). After 18 h, the cells were fixed with 4% PFA for 7 min and processed for immunofluorescence microscopy (Schneider et al. 2014), with Phalloidin AlexaFluor®568 (Molecular Probes).

Light Microscopy and Quantitative Assessment of COS7 Cell Membrane Topology

Confocal images were recorded using a Zeiss AxioObserver.Z1 microscope equipped with an ApoTome and AxioCam MRm CCD camera (Zeiss). Digital images were acquired as a z-series (0.2–0.3 µm intervals) by AxioVision Software (Vs40 4.8.2.0). Transfected cells with perimeters available for quantitative analysis of membrane topology were imaged in systematic sweeps across the coverslips using a Plan-Apochromat 63x/1.4oil objective. Quantitative image processing was done by ImageJ 1.46r software using maximum intensity projections of confocal image stacks at high magnification. The perimeter of each cell was outlined (segmented line tool) and the length determined (ROI manager). The number of protrusions from the cell perimeter (irrespective of their varying individual length) was determined and expressed per µm cell perimeter. In most cases, 15–27 cells were analyzed per condition in 3–4 assays reaching sum *n*-numbers of cells evaluated ranging from 54 to 87. The analyses of the srGAP2 F-BARdel25 mutant in comparison to wild-type and GFP control include only two assays and 32–34 cells per condition. Data is presented as mean + SEM. Statistical significance was calculated using Prism 5.03 software (GraphPad). Nonquantitative image processing was done by Adobe Photoshop.

Docking of Crystal Structures and Molecular Graphics

Docking of crystal structures into SAXS densities was performed manually using COOT (Emsley et al. 2010) and UCSF Chimera (Yang et al. 2012). Images were produced using Pymol (http://www.pymol.org) and UCSF Chimera.

Supplementary Material

Supplementary data are available at *Molecular Biology and Evolution* online.

Acknowledgments

We thank Adam Frost and Eckart Gundelfinger for valuable advice on the manuscript, Michaela Vogel, Lada Gevorkyan-Airapetov, Rinat Vasserman and Tomer Orevi for technical assistance, and Hadar Amartely and Mario Lebendiker for help with SEC-MALS experiments and analysis. Thanks to the staff of beamlines ID14, ID23, and ID29 of ESRF, and the staff of BESSY II BL14.1. This work was supported by funds from the ISF (Grants no. 182/10 and 1425/15 to Y.O.) and BSF (Grant no. 2013310, to Y.O. and Adam Frost) as well as by the DFG grants QU116/6-2 to B.Q. and KE685/4-2 to M.M.K.

References

Barak R, Opatowsky Y. 2013. Expression, derivatization, crystallization and experimental phasing of an extracellular segment of the human Robo1 receptor.*Acta Crystallogr Sect F Struct Biol Cryst Commun.* 69:771–775.

Beneken J, Tu JC, Xiao B, Nuriya M, Yuan JP, Worley PF, Leahy DJ. 2000. Structure of the Homer EVH1 domain-peptide complex reveals a new twist in polyproline recognition. *Neuron* 26:143–154.

Bianchi S, Stimpson CD, Bauernfeind AL, Schapiro SJ, Baze WB, McArthur MJ, Bronson E, Hopkins WD, Semendeferi K, Jacobs B, et al. 2013. Dendritic morphology of pyramidal neurons in the chimpanzee neocortex: regional specializations and comparison to humans. *Cereb Cortex.* 23:2429–2436.

Canagarajah B, Leskow FC, Ho JY, Mischak H, Saidi LF, Kazanietz MG, Hurley JH. 2004. Structural mechanism for lipid activation of the Rac-specific GAP, beta2-chimaerin. *Cell* 119:407–418.

Charrier C, Joshi K, Coutinho-Budd J, Kim JE, Lambert N, de Marchena J, Jin WL, Vanderhaeghen P, Ghosh A, Sassa T, Polleux F. 2012. Inhibition of SRGAP2 function by its human-specific paralogs induces neoteny during spine maturation. *Cell* 149:923–935.

Coutinho-Budd J, Ghukasyan V, Zylka MJ, Polleux F. 2012. The F-BAR domains from srGAP1, srGAP2 and srGAP3 regulate membrane deformation differently. *J Cell Sci.* 125:3390–3401.

Dauter Z. 2015. Solving coiled-coil protein structures. *IUCr J.* 2:164–165.

Dennis MY, Eichler EE. 2016. Human adaptation and evolution by segmental duplication. *Curr Opin Genet Dev.* 41:44–52.

Dennis MY, Nuttle X, Sudmant PH, Antonacci F, Graves TA, Nefedov M, Rosenfeld JA, Sajjadian S, Malig M, Kotkiewicz H, et al. 2012. Evolution of human-specific neural SRGAP2 genes by incomplete segmental duplication. *Cell* 149:912–922.

Elston GN, Benavides-Piccione R, DeFelipe J. 2001. The pyramidal cell in cognition: a comparative study in human and monkey. *J Neurosci.* 21:RC163.

Emsley P, Lohkamp B, Scott WG, Cowtan K. 2010. Features and development of Coot. *Acta Crystallogr D Biol Crystallogr*. 66:486–501.

Endris V, Haussmann L, Buss E, Bacon C, Bartsch D, Rappold G. 2011. SrGAP3 interacts with lamellipodin at the cell membrane and regulates Rac-dependent cellular protrusions. *J Cell Sci*. 124:3941–3955.

Fossati M, Pizzarelli R, Schmidt ER, Kupferman JV, Stroebel D, Polleux F, Charrier C. 2016. SRGAP2 and its human-specific paralog co-regulate the development of excitatory and inhibitory synapses. *Neuron* 91:356–369.

Fritz RD, Menshykau D, Martin K, Reimann A, Pontelli V, Pertz O. 2015. SrGAP2-dependent integration of membrane geometry and slit-Robo-repulsive cues regulates fibroblast contact inhibition of locomotion. *Dev Cell*. 35:78–92.

Frost A, Perera R, Roux A, Spasov K, Destaing O, Egelman EH, De Camilli P, Unger VM. 2008. Structural basis of membrane invagination by F-BAR domains. *Cell* 132:807–817.

Gilbert SF, Barresi MJF. 2016. Developmental biology, Chapter 26. 11th ed. Sunderland (MA): Sinauer Associates, Inc.

Guerrier S, Coutinho-Budd J, Sassa T, Gresset A, Jordan NV, Chen K, Jin WL, Frost A, Polleux F. 2009. The F-BAR domain of srGAP2 induces membrane protrusions required for neuronal migration and morphogenesis. *Cell* 138:990–1004.

Guez-Haddad J, Sporny M, Sasson Y, Gevorkyan-Airapetov L, Lahav-Mankovski N, Margulies D, Radzimanowski J, Opatowsky Y. 2015. The neuronal migration factor srGAP2 achieves specificity in ligand binding through a two-component molecular mechanism. *Structure* 23:1989–2000.

Harmand S, Lewis JE, Feibel CS, Lepre CJ, Prat S, Lenoble A, Boes X, Quinn RL, Brenet M, Arroyo A, et al. 2015. 3.3-million-year-old stone tools from Lomekwi 3, West Turkana, Kenya. *Nature* 521:310–315.

Kessels MM, Qualmann B. 2015. Different functional modes of BAR domain proteins in formation and plasticity of mammalian postsynapses. *J Cell Sci*. 128:3177–3185.

Kuwajima K. 1989. The molten globule state as a clue for understanding the folding and cooperativity of globular-protein structure. *Proteins* 6:87–103.

Mim C, Unger VM. 2012. Membrane curvature and its generation by BAR proteins. *Trends Biochem Sci*. 37:526–533.

Pertz OC, Wang Y, Yang F, Wang W, Gay LJ, Gristenko MA, Clauss TR, Anderson DJ, Liu T, Auberry KJ, et al. 2008. Spatial mapping of the neurite and soma proteomes reveals a functional Cdc42/Rac regulatory network. *Proc Natl Acad Sci USA*. 105:1931–1936.

Schneider K, Seemann E, Liebmann L, Ahuja R, Koch D, Westermann M, Hubner CA, Kessels MM, Qualmann B. 2014. ProSAP1 and membrane nanodomain-associated syndapin I promote postsynapse formation and function. *J Cell Biol*. 205:197–215.

Shimada A, Niwa H, Tsujita K, Suetsugu S, Nitta K, Hanawa-Suetsugu K, Akasaka R, Nishino Y, Toyama M, Chen L, et al. 2007. Curved EFC/F-BAR-domain dimers are joined end to end into a filament for membrane invagination in endocytosis. *Cell* 129:761–772.

Sporny M, Guez-Haddad J, Waterman DG, Isupov MN, Opatowsky Y. 2016. Molecular symmetry-constrained systematic search approach to structure solution of the coiled-coil SRGAP2 F-BARx domain. *Acta Crystallogr D Struct Biol*. 72:1241–1253.

Sudmant PH, Kitzman JO, Antonacci F, Alkan C, Malig M, Tsalenko A, Sampas N, Bruhn L, Shendure J, Genomes P, Eichler EE. 2010. Diversity of human copy number variation and multicopy genes. *Science* 330:641–646.

Wong K, Ren XR, Huang YZ, Xie Y, Liu G, Saito H, Tang H, Wen L, Brady-Kalnay SM, Mei L, et al. 2001. Signal transduction in neuronal migration: roles of GTPase activating proteins and the small GTPase Cdc42 in the Slit-Robo pathway. *Cell* 107:209–221.

Yamazaki D, Itoh T, Miki H, Takenawa T. 2013. srGAP1 regulates lamellipodial dynamics and cell migratory behavior by modulating Rac1 activity. *Mol Biol Cell*. 24:3393–3405.

Yang Z, Lasker K, Schneidman-Duhovny D, Webb B, Huang CC, Pettersen EF, Goddard TD, Meng EC, Sali A, Ferrin TE. 2012. UCSF Chimera, MODELLER, and IMP: an integrated modeling system. *J Struct Biol*. 179:269–278.

Zhang YE, Long M. 2014. New genes contribute to genetic and phenotypic novelties in human evolution. *Curr Opin Genet Dev*. 29:90–96.